Evaluation of Compliance of Arterial Vessel using Coupled Fluid Structure Interaction Analysis

Abhijit Sinha Roy[1], Lloyd H. Back[2] and Rupak K. Banerjee[3,4]

Summary

The *in vivo* and *ex vivo* compliance of arteries are expected to be closely related and estimated. Fluid-structure interaction analysis can assess the agreement between the two compliances. To evaluate this hypothesis, a pulsatile fluid-structure interaction analysis of blood flow in femoral artery of a dog was conducted using: (1) measured *in vivo* mean pressure (72.5 mmHg), mean pressure drop (0.59 mmHg), mean velocity (15.1 cm/sec); and (2) *ex vivo* measurements of non – linear elastic properties of femoral artery. Additional analyses were conducted for physiological pressures (104.1 and 140.7 mmHg) and blood flow using a characteristic linear pressure – flow relationship. The computed compliance decreased from 0.198% diameter change/mmHg at 72.5 mmHg to 0.145% diameter change/mmHg at 140.7 mmHg. The computed compliance tends to match well with *in vivo* compliance of femoral artery at lower pressure but is overestimated at higher pressure. This suggests an alteration in the compliance of the artery during *ex vivo* elasticity measurements.

keywords: Hemodynamics, fluid-structure interaction, femoral artery, pressure-flow relation, compliance.

Introduction

The compliance and non-linear elasticity of arterial wall have been researched for many years. Researchers have developed experimental setups to measure the circumferential, longitudinal moduli and the shear modulus of several arteries both in humans and animals [1-3]. Since arterial viscoelasticity is small, present modeling methods treat arteries primarily as elastic in nature. Several models have been proposed to quantify non-linear, isotropic and a few on anisotropic behavior of the arteries. Fluid-structure interaction is a valuable tool to analyze the effect of fluid stresses on wall mechanics in healthy and diseased arteries having plaque [4-8].

The issues of compliance mismatch and vessel injury are present in several clinical therapies, e.g., arterio-venous fistula having different artery and vein elasticity [9], balloon angioplasty causing stretching of the artery [10,11], migration and endoleaks in endovascular grafts [12,13], stents alter the compliance of the

[1]Cleveland Clinic Cole Eye Institute

[2]Jet Propulsion Laboratory, California Institute of Technology, Pasadena, CA, USA

[3]Department of Biomedical Engineering, University of Cincinnati, OH, USA

[4]Corresponding Author: R. K. Banerjee, Department of Mechanical, Industrial and Nuclear Engineering, 688 Rhodes Hall, PO Box 210072, Cincinnati, OH 45221; Tel: 513-556-2124; Fax: 513-556-3390; email: rupak.banerjee@uc.edu

vessel [14,15]. *To reproduce the in vivo hemodynamics and wall mechanics, it is essential to know whether the arterial properties measured ex vivo are indicative of properties that exist in vivo.* Therefore, this study aims to compare the *in vivo* compliance of an artery based on elastic properties measured *ex vivo*. In this study, this comparison has been performed for a range of systemic pressures and blood flow, which is characteristic of pressure dependent alterations in blood flow in femoral artery of dog. This study utilizes *in vivo* measurements of pressure, pressure drop, velocity and cross-sectional area in femoral artery of dog and a computational fluid structure-interaction model using non-linear, anisotropic wall properties for the same vessel. The computed wall mechanics are compared with *in vivo* compliance of the femoral artery of dog reported elsewhere.

Methods

In Vivo experiment

The experimental measurements are shown in Figure 1 [16]. Figure 2 shows a schematic diagram of the femoral artery, with dimensions and locations of the pressure taps and flow cuff [16]. The femoral artery tapers linearly along its length. At the inlet and outlet (figure 2), there was a small branch, which was used as a pressure tap and connected via tubing to the pressure transducer. The flow was measured by an external Doppler flow cuff as shown in the figure. The time averaged pressure drop $(\Delta\tilde{p})$ measured experimentally between the two pressure taps (inlet and outlet) was 0.59 mmHg. The time and spatially averaged axial velocity $(\tilde{u}_z)$ measured by the cuff was 15.1 cm/sec. Mean blood pressure was 72.5 mmHg. The heart rate was 128 beats/min (period T = 0.469 sec).

Compliant artery - blood flow model
Geometry

The mean inner wall diameter at the inlet $(\tilde{d}_i)$ and outlet $(\tilde{d}_o)$ is 3.8 and 3.6 mm, respectively. The *in situ* axial distance between the pressure taps is 5.2 cm, such that the ratio of axial length to diameter is around 13.7 [16].

Blood flow model

The blood flow through the femoral artery is laminar, incompressible, viscous, pulsatile and non-Newtonian. An axi-symmetric form of the governing equations is solved. The following equations are used:

$$\nabla . u = 0 \text{ (continuity equation)} \tag{1}$$

$$\rho(\partial u/\partial t + ((u - u_m).\nabla u) = -\nabla p + \nabla.(\mu \nabla u) \text{ (momentum equation)} \tag{2}$$

The Carreau model of non-Newtonian blood viscosity is used [16]:

$$\mu = \mu_\infty + (\mu_0 - \mu_\infty) . \left(1 + (\beta\dot{\gamma})^2\right)^{(n-1)/2} \tag{3}$$
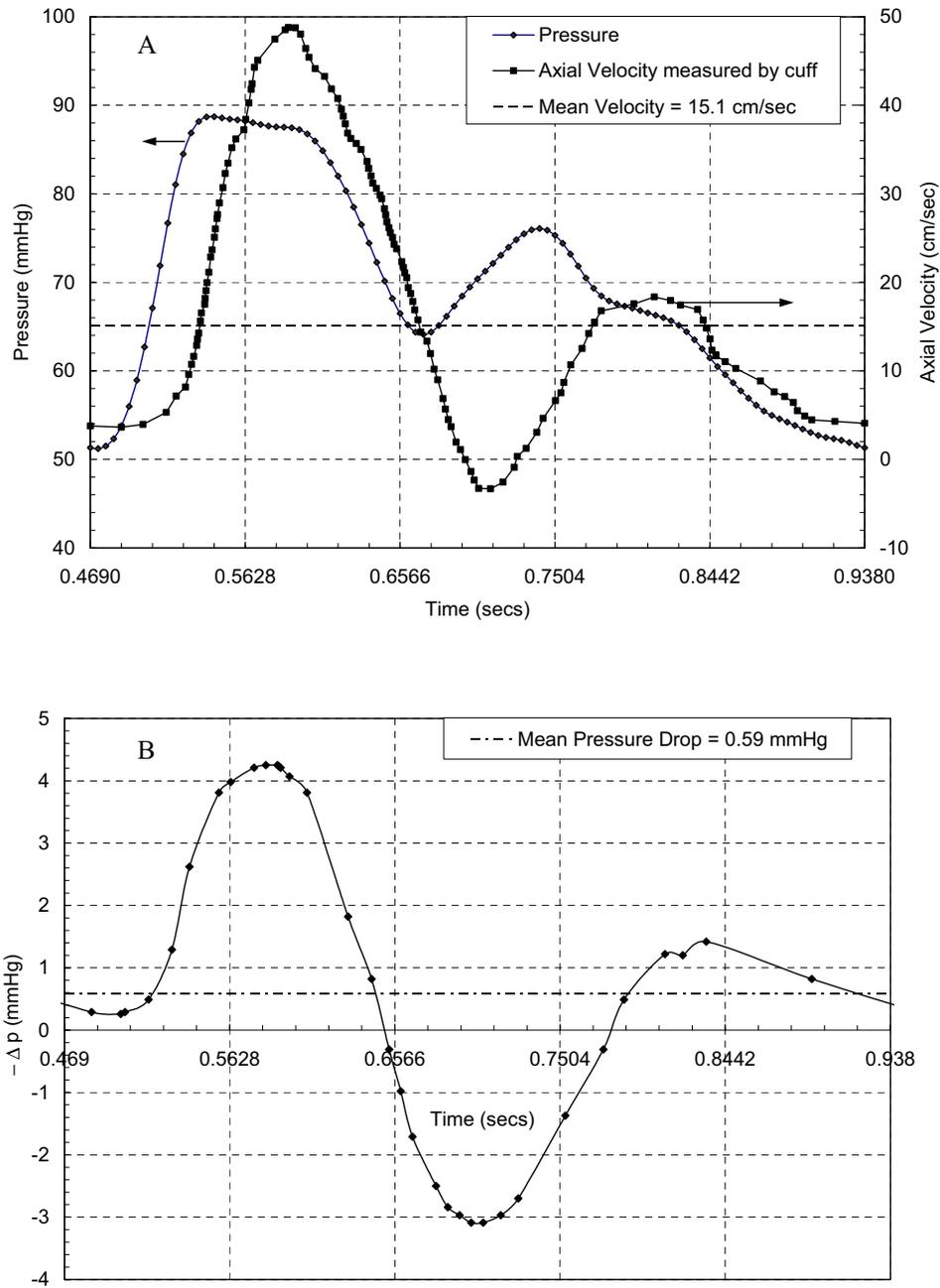
Figure 1: (A) Experimental pressure and axial velocity measured in the tapered femoral artery of dog; (B) Measured *in vivo* pressure drop measured between the inlet and outlet of the tapered artery section.

where μ_∞ =0.0345 Poise, μ_0 =0.56 Poise, β =3.313 sec and n = 0.3568. The density (ρ) of blood is 1.05 gm/cm^3.

The boundary conditions are as follows (Figure 2):

$$p \text{ at the inlet } = p_i(t) \tag{4}$$

$$p \text{ at the outlet } = p_o(t) \tag{5}$$

$$u_r \text{ at the axis } = 0 \tag{6}$$

$$\partial u/\partial z = 0 \text{ at the inlet and outlet} \tag{7}$$

$$\tag{8}$$

where u_m, u_r and u is the mesh velocity, radial velocity and velocity vector, respectively. At lumen and arterial wall interface, no slip boundary condition is applied:

$$u = \dot{d}^S \tag{9}$$

where $\dot{d}^S$ is the time derivative of displacement at blood - inner wall (of the artery) interface.

Arterial wall model

The arterial wall is assumed to be homogenous, hyperelastic and incompressible. The equilibrium equations and boundary conditions for the arterial wall are as follows:

$$\sigma^S_{\alpha\beta,\beta} = 0 \tag{10}$$

$$d^S = d^F \text{ at the inner wall} \tag{11}$$

$$\sigma^S_{\alpha\beta}.n_\beta = 0 \text{ at the outer wall} \tag{12}$$

$$\sigma^S_{\alpha\beta}.n_\beta = \sigma^F_{\alpha\beta}.n_\beta \text{ at the fluid-solid interface} \tag{13}$$

where d^S, d^F, $\sigma^S_{\alpha\beta}$ and $\sigma^F_{\alpha\beta}$ are the displacement and stress tensors for the arterial wall and blood flow, respectively, and n is a unit vector normal to the boundary. The radial displacement of the axis is zero. The *in vivo* length of the artery is 5.2 cm. The cauchy circumferential and longitudinal stress - stretch ratio data for the dog femoral artery are used as shown in figure 3A [17]. Only the average values of *ex vivo* stresses were reported by Attinger [17], measured from cylindrical samples of dog femoral artery of 6 cm *in situ* length. The Mooney-Rivlin model for incompressible solid has been used. The strain energy density function (W: eq. 13) is expressed as function of I_1 and I_2 (see eq. 13), where I_1 and I_2 are the first and second strain invariants, respectively.

$$W = C_1 (I_1 - 3) + C_2 (I_2 - 3) + C_3 (I_1 - 3)^2 + C_4 (I_1 - 3)(I_2 - 3) + C_5 (I_2 - 3)^2 \tag{14}$$
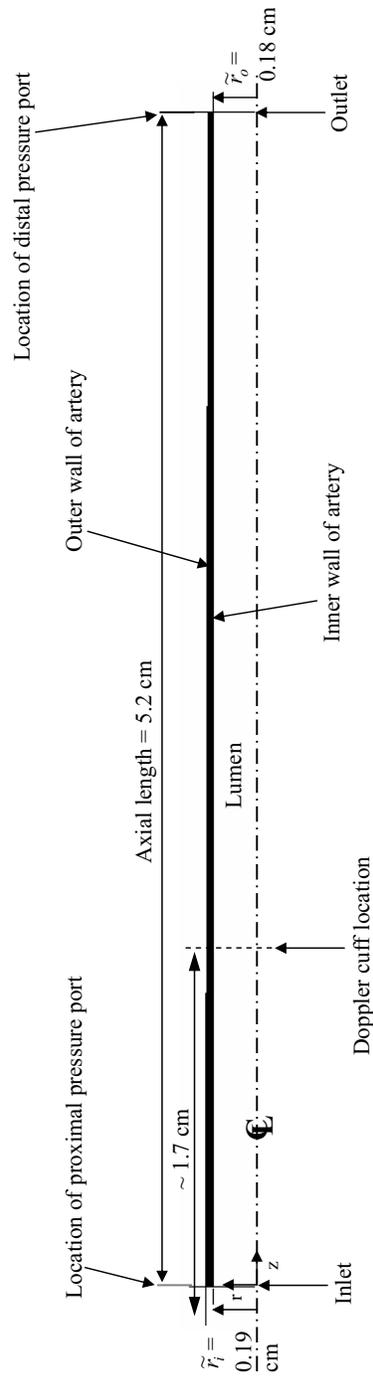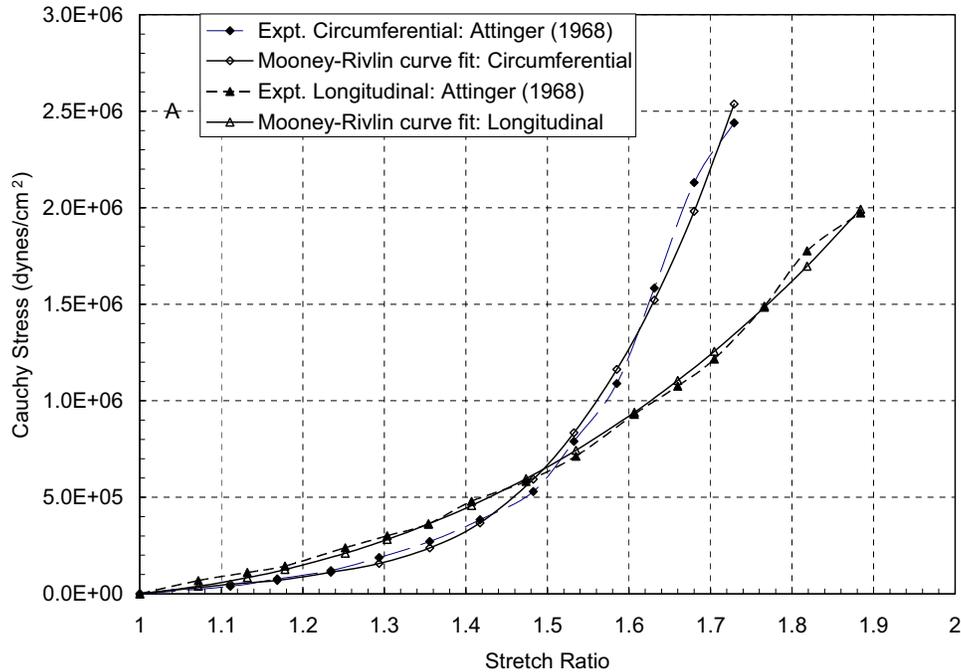
Figure 2: Geometry of tapered femoral artery of dog. Dimensional values reported are mean values obtained from angiographic images. Figure shows an axisymmetric model of the artery.

From eq. 13, the cauchy $(\sigma^c_{\alpha\alpha})$ principal stresses are given by:

$$\sigma^c_{\alpha\alpha} = \lambda_\alpha (\partial W / \partial \lambda_\alpha) \tag{15}$$

Here, C_j's are the material constants obtained by curve fitting the experimental data [17]. For an incompressible artery, $\lambda_r \lambda_\theta \lambda_z = 1$. For curve fitting the circumferential stress – stretch ratio data, it has been assumed that $\lambda_r = \lambda_\theta = \lambda$ and $\lambda_z = \lambda^{-2}$ where λ is the corresponding circumferential stretch ratio. For curve fitting the longitudinal stress – stretch ratio data, it has been assumed that $\lambda_z = \lambda'$ and $\lambda_r = \lambda_\theta = \lambda' - (1/2)$ where λ' is the corresponding longitudinal stretch ratio. These assumptions describe the implemented experimental protocols by Attinger [17]. The data was obtained from the no – load configuration, i.e., when transmural pressure is zero and corresponding stresses in the artery are zero, assuming residual stresses are not present in the wall [17].

Thus, the error function ε has been minimized using the Nelder – Mead minimization algorithm to obtain the material constants:

$$\varepsilon^2 = \sum_{i=1}^{n} \left[(\sigma_{\theta\theta} - \sigma^*_{\theta\theta})^2_i + (\sigma_{zz} - \sigma^*_{zz})^2_i \right] \tag{16}$$

where σ and σ^* are the curve fit and measured *ex vivo* values [17] of stresses, respectively. The index i represents the ith of n data points. As a measure of goodness
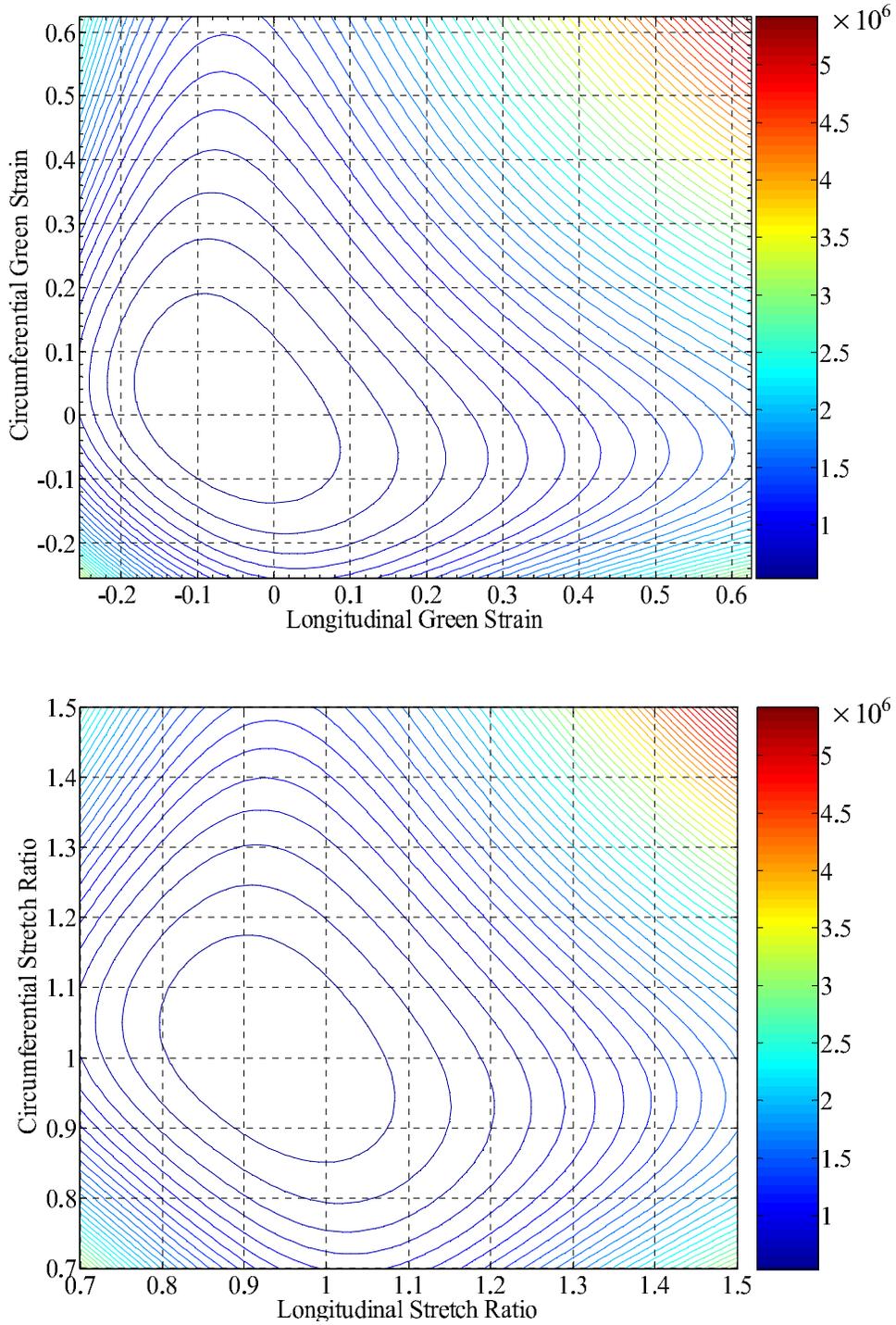
Figure 3: (A) Non-linear circumferential and longitudinal stress-stretch ratio data. The Mooney-Rivlin model, regressed to this experimental data, is shown as a solid line; (B) Plot showing convexity of Mooney-Rivlin material model using regressed material constants for the femoral artery of dog.

of fit, the R^2 value of 0.98 has been achieved for both the circumferential and longitudinal stress data (figure 3A). The curve fitting procedure provided the following material constants: $C_1 = 296220$ dynes/cm^2, $C_2 = $ -221950 dynes/cm^2, $C_3 = 27166$ dynes/cm^2, $C_4 = 35681$ dynes/cm^2, $C_5 = $ -3686 dynes/cm^2. To check the stability of this curve fit, the contours of W have been plotted as function of both stretch ratio and Green strain (Figure 3B). As seen in figure 3B, the convexity of contour plot of W ensures the stability of the compliant wall - blood flow computations performed in this study [18].

Hemodynamic pressure – flow relation for the femoral artery of dog

The linear pressure – flow relationship for femoral artery of dog at resting and vasodilated flow [19-21] is used to estimate the blood flow at different pressures ($\tilde{p}_o$). Ehrlich et al. [19] have measured a zero – flow pressure of 35.4 mmHg at resting flow in femoral artery of dogs, .i.e., when pressure approaches 35.4 mmHg, blood flow in the artery ceases. Using our *in vivo* data and the zero – flow pressure of 35.4 mmHg, a linear line is regressed (figure 4A). Two different pressure profiles are used with mean values ($\tilde{p}_o$) of 104.1 [22] and 140.7 mmHg [23] to compute the compliance at higher $\tilde{p}_o$. The time period of elevated pressure waveforms is 0.469 sec [16]. At the elevated $\tilde{p}_o$, the corresponding flow rate is obtained by extrapolating the linear pressure – flow line (Figure 4A), and is 188.2 and 289.8 ml/min, respectively.

Computation procedure

The details of the computation procedures are as follows:

a) *In vivo* measurements: Baseline case

At the outlet, the time varying pressure is prescribed as normal traction. However, the experimental velocity profile, measured distal to the inlet, does not account for radial variation of the local axial velocity. However, both a temporal and spatially varying velocity $u_z(r,t)$ profile is required as a boundary condition. To specify the boundary conditions similar to the *in vivo* measurements, the following procedure has been adopted:

(1) First in a rigid artery model with dimensions as shown in Figure 2, the pressure drop, $\Delta p(t)$, is computed by specifying temporal and spatial dependent axial velocity profile at the inlet and our measured *in vivo* $p_o(t)$, having mean value of 72.5 mmHg, at the outlet. At any time t, a parabolic velocity profile for a Newtonian liquid is used to describe the spatial variation of axial velocity.

(2) Since $\Delta \tilde{p}$ in a compliant vessel is different than $\Delta \tilde{p}$ in a rigid vessel, a constant number is added to each instantaneous computed $\Delta p(t)$ obtained from the rigid artery model. This provides an adjusted time averaged pressure drop ($\Delta \tilde{p}$),
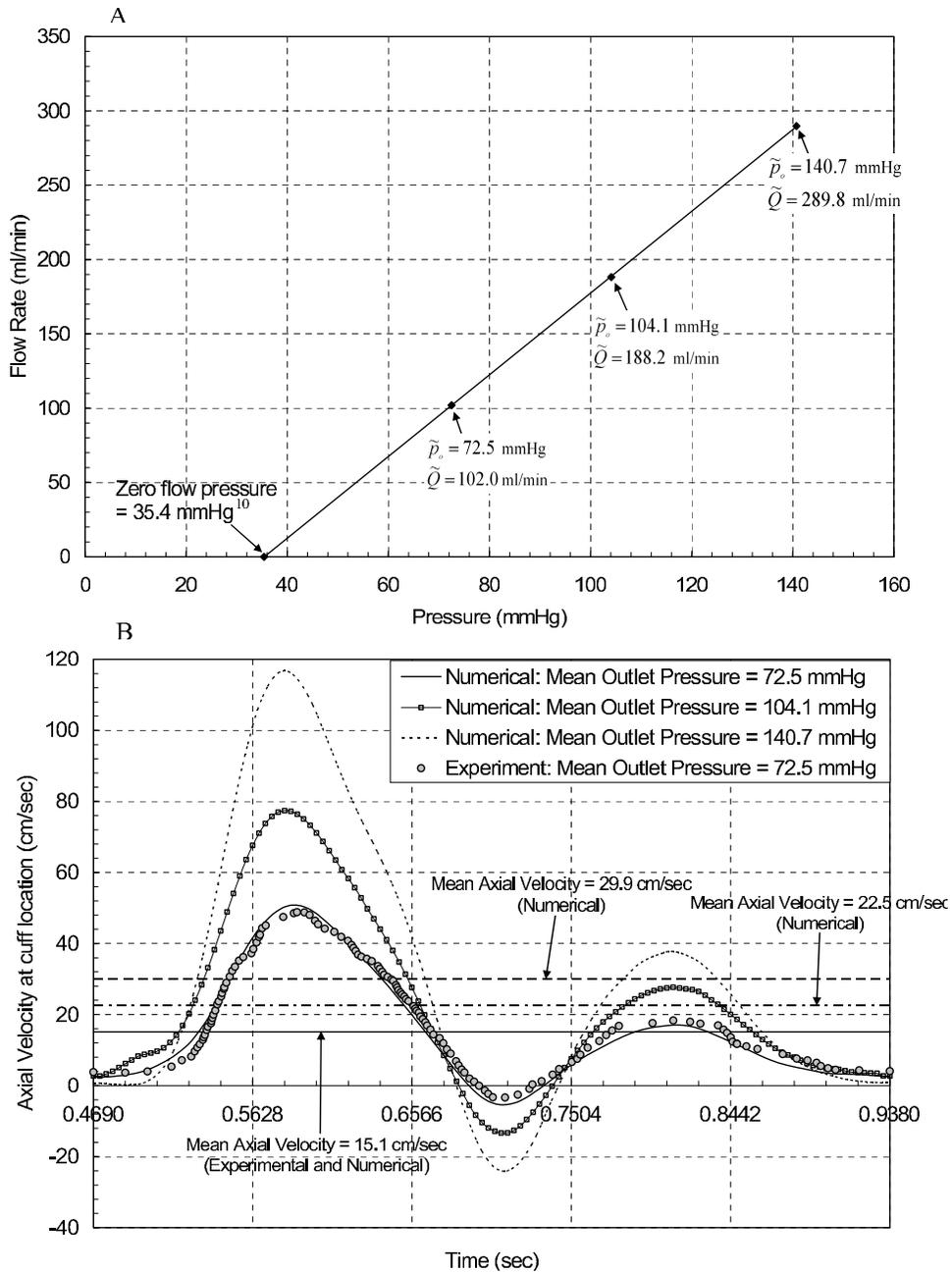
Figure 4: Estimation of flow using linear pressure - flow relationship: (A) Extrapolated linear pressure - flow relationship for baseline and elevated pressure; (B) Measured *in vivo* and computed spatially averaged axial velocity profiles at cuff location.

which is higher than that computed from the rigid artery model. The positive number is chosen using an iterative procedure where multiple computations are performed till $\tilde{u}_z = 15.1$ cm/sec, similar to our *in vivo* measurements (Figure 1), is obtained at the cuff location.

(3) Then, the computed (from the rigid artery model) and incremented (after adding the positive number) $\Delta p(t)$ is added to the *in vivo* pressure $p_o(t)$ at the outlet to obtain the pressure $p_i(t)$ at the inlet.

(4) The resultant $p_i(t)$ is specified as normal traction at the inlet while our measured *in vivo* $p_o(t)$ [16] is prescribed as normal traction at the outlet for the computation.

For the compliant model, the artery was first stretched by 48% of its initial length [24,25] such that the final length is 5.2 cm, the *in vivo* length. The no - load radius at the inlet and outlet are adjusted such that the computed $\tilde{d}_i$ and $\tilde{d}_o$ is 0.38 and 0.36 cm, respectively. Further, the wall thickness at no - load is adjusted such that the ratio of wall thickness (t) to radius (r) is about 0.14 [3].

b) Elevated pressure and flow

For the elevated pressure profiles, the adjusted time averaged pressure drop $(\Delta \tilde{p})$ obtained from the baseline case is multiplied by a factor (> 1) to increase its value to $\Delta \tilde{p}_e$. The value is increased till the computed mean flow rate at the cuff location is 188.2 ml/min and 289.8 ml/min for $\tilde{p}_o$ of 104.1 and 140.7 mmHg, respectively (Figure 4B and 5A). Thus, the procedure used for these computations is as follows:

(1) First, the compliant artery is stretched to its *in vivo* length as described in baseline case.

(2) Then, the $\Delta p_e(t)$ is added to the pressure $p_o(t)$ (pressure profiles with mean values of 104.1 and 140.7 mmHg) at the outlet to obtain the corresponding pressure $p_i(t)$ at the inlet.

(3) Then, the new $p_i(t)$ is specified as normal traction at the inlet while the elevated $p_o(t)$ is prescribed as normal traction at the outlet.

(4) Multiple computations are performed till values of $\Delta p_e(t)$ and $p_i(t)$ satisfy the estimated flow from the extrapolated linear pressure –flow relationship for corresponding $\tilde{p}_o$ of 104.1 and 140.7 mmHg, respectively.

Using this procedure, the computed $\bar{u}_z$ profiles at the cuff location for the elevated pressures are similar in shape to our *in vivo* measured pulse (Figure 4B). The no – load inlet radius, outlet radius and wall thickness have been kept the same for these computations as those for the baseline case.

Mesh and convergence

The finite element method has been used to solve the blood flow and arterial wall equations simultaneously [26]. The mesh consists of bilinear, quadrilateral, axi-symmetric elements. The number of nodes in the blood and arterial wall zone are 1515 and 1000, respectively. Mesh independency has been checked till the solutions for two different mesh sizes differed by less than 0.5%. The convergence criteria for the fluid and solid degrees of freedom are 10^{-6} and 10^{-7}, respectively. The 2nd order trapezoidal rule is used for time integration of the blood flow and arterial wall mechanics equations. A fixed time step size of 2.345×10^{-4} sec is used. Each computation is run for 3 cycles. It is observed that the solution remain unchanged after the first cycle. Thus, only results from the second cycle are presented in this paper.

Results

Velocity profiles and pressure drop

The spatially averaged axial velocity profiles $\bar{u}_z(t)$ are plotted in figure 4B for baseline and elevated pressure $\tilde{p}_o$. The computed $\tilde{\bar{u}}_z$ are 22.5 cm/sec and 29.9 cm/sec for $\tilde{p}_o$ of 104.1 and 140.7 mmHg, respectively; a 49% and 98% increase from a measured value of 15.1 cm/sec for the baseline case. As seen in figure 4B, the axial velocity profiles at different t are similar, though they differ in magnitude for baseline and elevated pressure. The close agreement between our *in vivo* [16] and computed data for $\tilde{p}_o = 72.5$ mmHg provides confidence to our estimates for $\bar{u}_z$ at different t for the elevated pressures. The Womersley number [27] for the baseline calculation is 3.7 which increases to 4.2 for the elevated pressure.

Figures 5A shows the baseline and elevated $\tilde{p}_o$ vs. t. These profiles have been used for the compliant wall – blood flow computations. The corresponding $-\Delta p(t)$ $(= p_i(t) - p_o(t))$ profiles for the baseline and elevated pressure at different t are shown in figure 5B. It can be seen that all $-\Delta p(t)$ are similar in shape but differ in magnitude. A significant increase in instantaneous pressure drop is seen with increasing $\tilde{p}_o$, flow and the diameter of the vessel. The *in vivo* peak $-\Delta p(t)$ during systolic and diastolic forward flow is 4.25 and 1.5 mmHg, respectively (Figure 1). Comparing the baseline case and *in vivo* measurement, peak Δp during systole is 29% lower, and during diastolic forward flow is 31 % lower. If the time averaged $-\Delta \tilde{p}$'s are compared, then computed value for the baseline case is 0.72 mmHg as compared to 0.59 mmHg measured *in vivo*; a difference of 18%. Thus, the difference in $-\Delta \tilde{p}$ is significantly lower than instantaneous $-\Delta p(t)$. The

computed $-\Delta \tilde{p}$ is 1.06 mmHg and 1.35 mmHg for $\tilde{p}_o$=104.1 and 140.7 mmHg, respectively.

All the computations show significant phase difference between *in vivo* and computed $-\Delta p(t)$. On an average, the phase difference between the *in vivo* and computed $-\Delta p(t)$ is 20 degrees for the baseline case. The phase difference between computed $-\Delta p(t)$ and measured $\bar{u}_z(t)$ [16] for the baseline case, which is ~ 26.6 degree. This is consistent with Womersley theory for pulsatile blood flows [27]. The phase difference between the computed $-\Delta p(t)$ and *in vivo* $-\Delta p(t)$ [16] is due to response limitation of diaphragm based pressure transducer, which was available to the authors and used for the *in vivo* experiment. However, the $-\Delta \tilde{p}$ value is not affected much if time averaging is done synchronized with the heart rate. Table 1 summarizes the results of the computations, with mean values of $\tilde{d}_i$, $\tilde{d}_o$, $t\tilde{h}_i$ and $t\tilde{h}_o$.

Table 1: Summary of mean pressure drop ($\Delta \tilde{p}$), mean axial velocity ($\tilde{\bar{u}}_z$), mean radius at inlet ($\tilde{d}_i$) and outlet ($\tilde{d}_o$), wall thickness at inlet ($\tilde{t}_i$) and outlet ($\tilde{t}_o$) for baseline and elvated pressures.

	$-\Delta\tilde{p}$ (mmHg)	$\tilde{\bar{u}}_z$ (cm/sec)	$\tilde{d}_i$ (cm)	$\tilde{d}_o$ (cm)	$t\tilde{h}_i$ (cm)	$t\tilde{h}_o$ (cm)
In vivo[4]	0.59	15.1	0.38	0.36	-	-
$\tilde{p}_o = 72.5$ mmHg (Numerical)	0.72	15.1	0.38	0.36	0.027	0.027
$\tilde{p}_o = 104.1$ mmHg (Numerical)	1.06	22.5	0.41	0.39	0.026	0.026
$\tilde{p}_o = 140.7$ mmHg (Numerical)	1.35	29.9	0.44	0.42	0.024	0.024

Compliance of the femoral artery of dog

Due to variability in artery dimensions, wall thickness and hemodynamic conditions ,compliance is a useful parameter to compare experimental data using computational models. Compliance (c) of a vessel is given as follows [28]:

$$c = \left(\frac{1}{r}\right)\left(\frac{\partial p}{\partial r}\right)^{-1} \tag{17}$$

Figure 6A-C show the variation of mid-wall radii at the inlet and outlet for the baseline and elevated pressures. Many researchers have linearised eq. 16 to estimate a simple measure of c for a given pressure and flow pulse, expressed as percent:

$$c = \frac{[d(\max) - d(\min)]}{d(\min) \times [p(\max) - p(\min)]} \times 100 \tag{18}$$

Here $d(\max)$ and $d(\min)$ are the maximum and minimum diameter at $p(\max)$ and $p(\min)$, respectively. The values of c at the inlet and outlet have been calculated and compared with *in vivo* data published for femoral artery of dog [29].
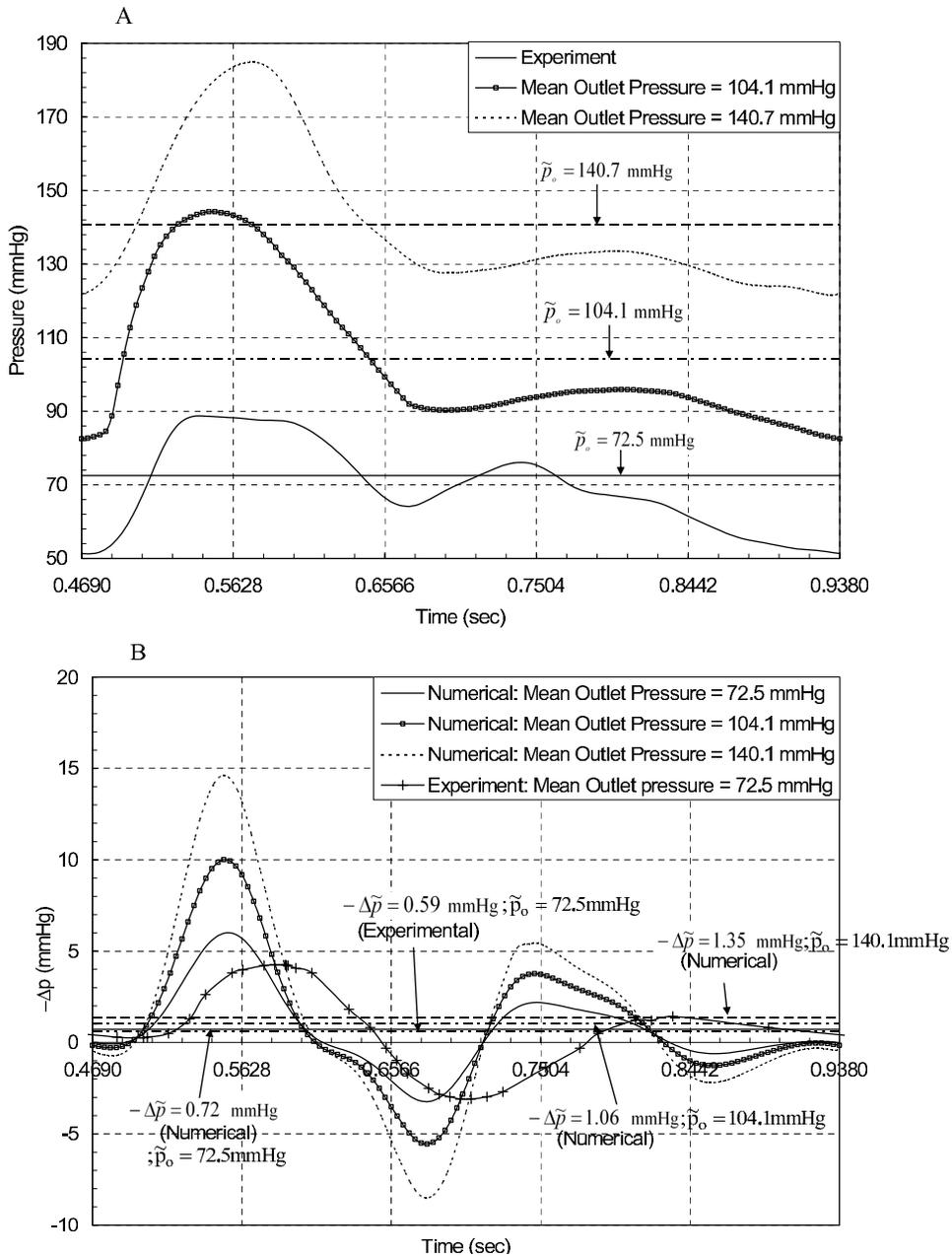
Figure 5: (A) Measured *in vivo* pressure profiles: baseline and elevated; (B) Measured *in vivo* and computed pressure drop between inlet and outlet.

Megerman et al. [29] measured *in vivo* the compliance, using only the outer wall diameter, in dissected and undissected femoral artery of mongrel dog. For the
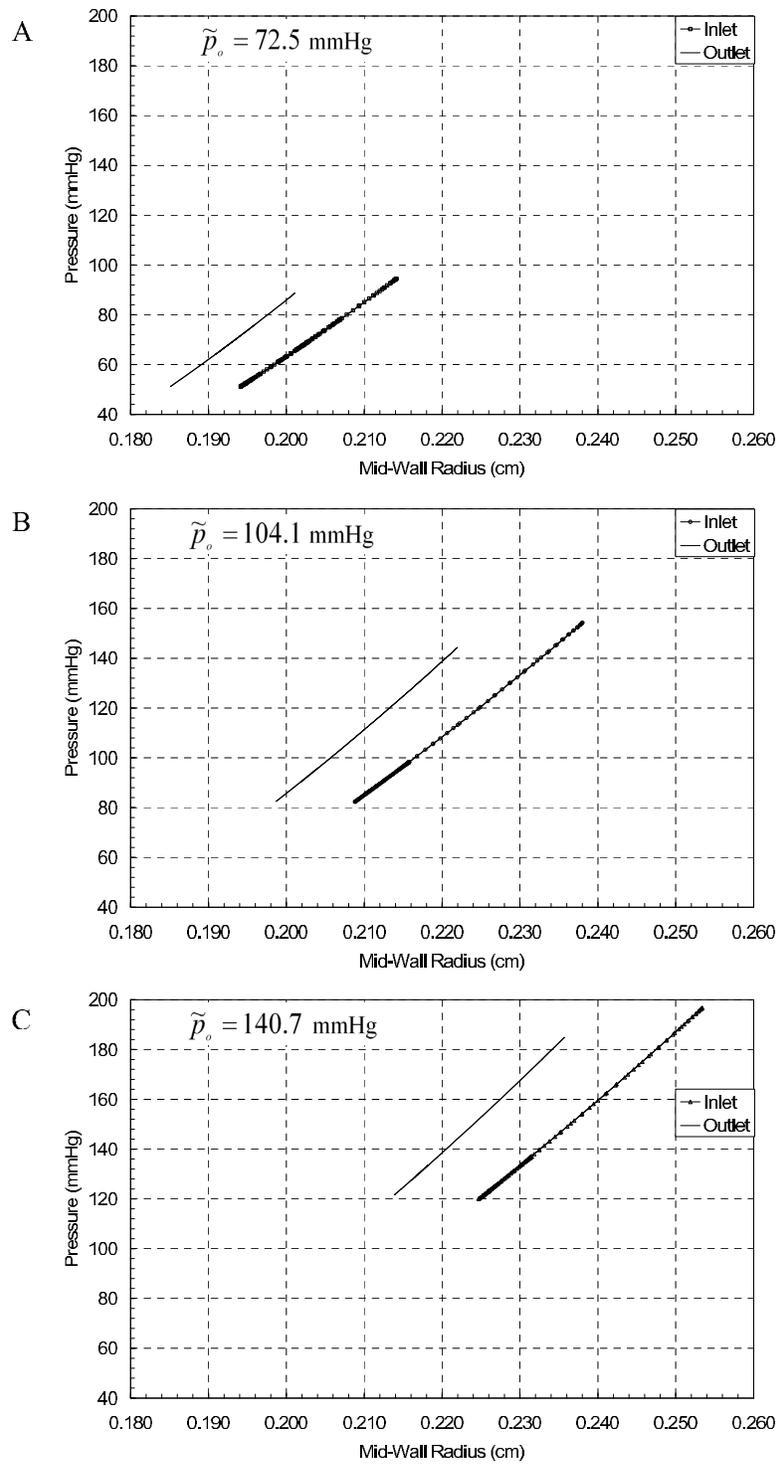
Figure 6: Pressure vs. mid - wall radius curves at inlet and outlet: (A) $\tilde{p}_o$ = 72.5 mmHg; (B) $\tilde{p}_o$ = 104.1 mmHg; (C) $\tilde{p}_o$ = 140.7 mmHg.

present computations, table 2 summarizes the maximum and minimum outer wall diameters and pressures (from figure 6A-C) at the inlet and outlet. Here, dissection implies that the artery is dissected free from the surrounding tissue similar to *ex vivo* conditions (figure 7). In figure 7, the computed *c* decreases from 0.198% diameter change/mmHg for $\tilde{p}_o$= 72.5 mmHg to 0.145% diameter change/mmHg for $\tilde{p}_o$= 140.4 mmHg. In comparison with *in vivo* data [29], the *c* tends to match at lower pressure (~70-110 mmHg) and is overestimated at higher pressure by our computations (figure 7). The compliance of dissected artery is lower than undissected artery [29]. This suggests an alteration in the vascular wall mechanics of the artery from the *in vivo* conditions. The strong dependence of *c* on pressure is evident.
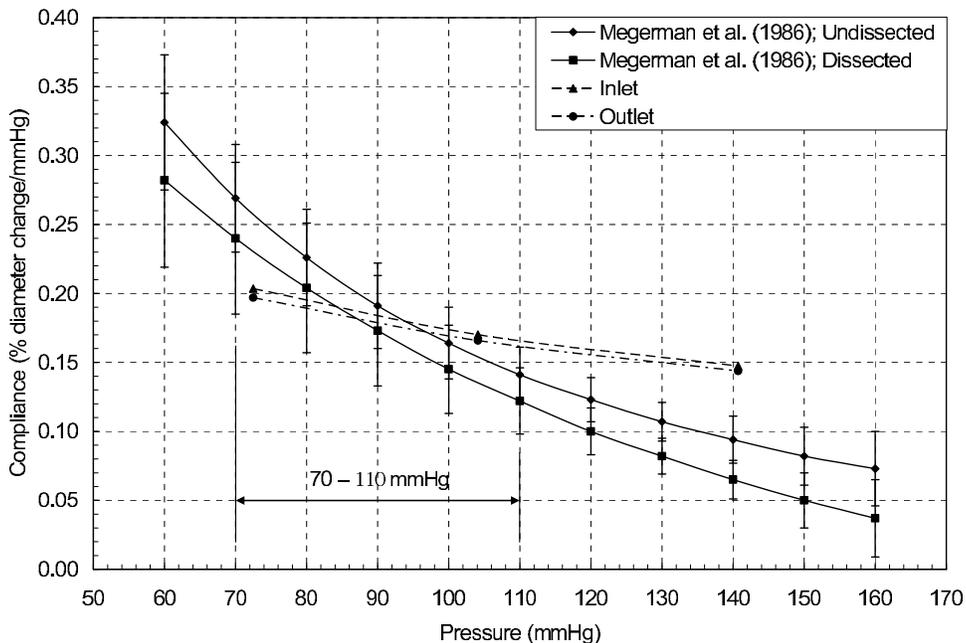

Figure 7: Compliance vs. pressure evaluated at inlet and outlet. The computed data is compared with *in vivo* data from reference.

Stress at the mid-wall radius

   Figure 8 shows the cauchy circumferential and longitudinal stress vs. time for baseline and elevated pressures at mid wall radius both at the inlet and outlet. The phasic variation in circumferential stress and longitudinal stress (at the inlet) is identical to the pressure profile. In contrast, the longitudinal stress at the oulet is inverted in shape for all the computations. The mean circumferential stress increases from 42 kPa for $\tilde{p}_o$= 72.5 mmHg to 146 kPa for $\tilde{p}_o$= 140.7 mmHg. In contrast, the mean values of longitudinal stresses are considerably lower, which are 28 kPa and

Table 2: Calculated compliance of the femoral artery at different pressures along with maximum and minimum outer wall diameter and pressure.

	c (% diameter change /mmHg)	Outer wall d(cm), p_i (mmHg) at inlet		Outer wall d(cm), p_o (mmHg) at outlet	
		Min.	Max.	Min.	Max.
$\tilde{p}_o = 72.5$ mmHg	~ 0.198	0.420, 51.3	0.456, 94.5	0.402, 51.3	0.432, 88.7
$\tilde{p}_o = 104.1$ mmHg	~ 0.168	0.448, 82.3	0.502, 154	0.427, 82.5	0.471, 144.2
$\tilde{p}_o = 140.7$ mmHg	~ 0.145	0.478, 121.3	0.531, 196.7	0.456, 121.8	0.498, 184.9

31 kPa, respectively. In the physiological pressure range of 100 mmHg, the circumferential stresses should be in the range of 50-100 kPa under *in situ* pre-stretch conditions [25,30]. The present calculation for $\tilde{p}_o = 104.1$ mmHg (mean circumferential stress value of 92 kPa) using our material model equation agrees well with the past studies [25,30].

Discussion and Conclusion

In this study, the reproducibility of *in vivo* compliance of femoral artery of a dog from *ex vivo* measured wall properties has been studied. While the computations predict radial dilations and stress distributions similar to *in vivo* values, the compliance of the vessel differs from its *in vivo* value. The use of linear equation (eq. 17) to calculate compliance is justified since Megerman et al. [29] have also used the same equation. Our estimates for c and *in vivo* measurements for femoral artery of dog match well in the pressure range of 70 mmHg to 110 mmHg but are higher for pressures above 110 mmHg.

In this study, the effect of residual stresses is not considered since such information was not reported by Attinger [17]. A recent fluid-structure interaction study on removal of tethering suggests that dissection of surrounding tissue from the arterial wall (as in *ex vivo* measurements) produces native changes in the elastic properties of the artery itself.[8]. The present analyses supports the conclusions made by Zhang and colleagues [8] and provides direct comparison between *in vivo* and *ex vivo* elasticity data. Cox et al. [31] have reported that the viscoelastic contribution to the dynamic elastic modulus of the femoral artery of dog is less than 2%. Thus, viscoelasticity should have negligible impact on the calculated compliance in this study. Studies where *in vivo* hemodynamics, compliance and *ex vivo* elastic properties have been measured are rare, if not non - existent. Further, experimental protocols tend to differ among studies [2,32]. Therefore, standardized *ex vivo* experimental techniques for measurement of arterial wall properties are needed. Presently, there are few layer specific models available that are able to account for
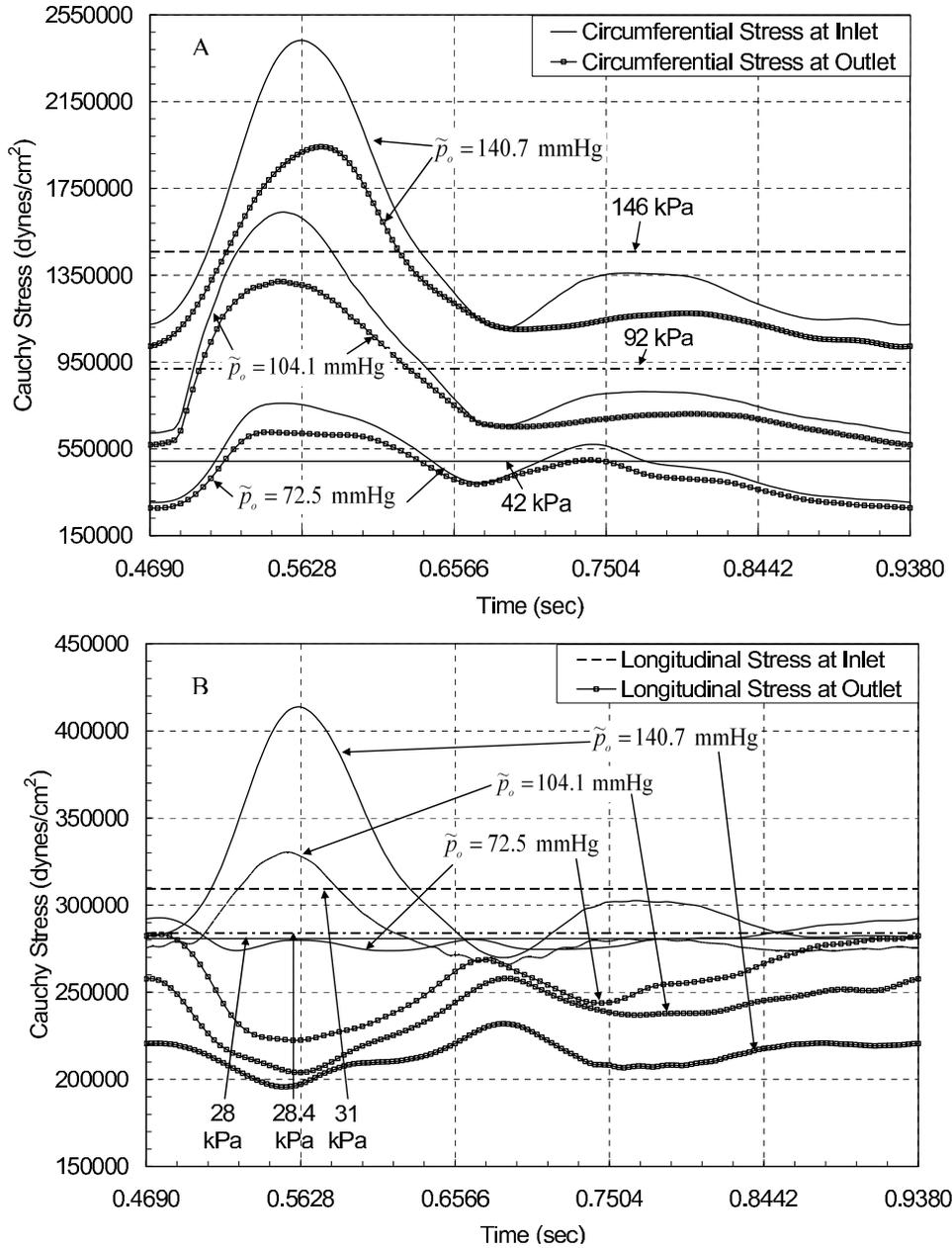
Figure 8: (A) Circumferential stress vs. time for baseline and elevated pressures at inlet and outlet; (B) Longitudinal stress vs. time for baseline and elevated pressures at inlet and outlet. Mean stress values at the inlet are shown by horizontal lines.

directional orientation of elastin and collagen fibres [e.g., 10]. Data pertaining to material constants for regressed layer - specific model equations for animals are limited. These future studies should compare both pulsatile hemodynamics and vascular properties measured *ex vivo* for normal and diseased arteries to *in vivo* compliance of the arteries.

Acknowledgement

Nomenclature

p	pressure in mmHg	F	fluid (blood flow)
d	diameter in cm	c	Cauchy
r	radius in cm	l	Lagrange
t	time in sec	.	time derivative
c	compliance in %diameter change/mmHg	*	experimental data
		Subscripts	
λ	stretch ratio	z	axial
σ	stress in dynes/cm^2	r	radial
n	number of data points	θ	circumferential
th	wall thickness	α, β	co-ordinate directions
Superscripts		i	inlet
$-$	spatially averaged	o	outlet
$\sim$	time averaged		

References

1. Fung, Y. C. (1997) in Biomechanics: Circulation. (Springer-Verlag, NY).

2. Humphrey, J. D. (2002) in Cardiovascular solid mechanics: cells, tissues, and organs, 1st edition, (Springer-Verlag, NY).

3. Nichols, W.M.; O' Rourke, M.F. (2005) in McDonalds blood blow in arteries. Theoretical, experimental and clinical principles, Fifth edition, (Hodder Arnold, UK,).

4. Bathe, M.; Kamm, R.D. (1999) ASME J. Biomech. Eng. 121, 361-369.

5. Dutta, A.; Tarbell, J.M. (1996) ASME J. Biomech. Eng. 118, 111-119.

6. Tang, D.; Yang, C.; Kobayashi, S.; Ku, D.N. (2004) ASME J. Biomech. Eng. 126, 363-70.

7. Tang, D.; Yang, C.; Zheng, J.; Woodard, P.K.; Sicard, G.A.; Saffitz, J.E.; Yuan, C. (2004) Ann. Biomed. Eng. 32, 947-960.

8. Zhang, W.; Herrera, V.; Atluri, S.N.; Kassab, G.S. (2004) ASME J. Biomech. Eng. 126:760-769.

9. Migliavacca, F.; Dubini, G. (2005) Biomech. Model. Mechanobiol. 3, 235-250.

10. Holzapfel, G.A.; Sommer, G.; Gasser, C.T.; Regitnig, P. (2005) Am. J. Physiol. Heart. Circ. Physiol. 289, H2048-2058.

11. Rogers, C.; Tseng, D.Y.; Squire, J.C.; Edelman, E.R. (1999) Circ. Res. 84, 378–383.

12. Ferrar, D.W., Roberts, A.K., Lawrence-Brown, M.M., McLellan, D., Semmens, J.B. (2005) J Endovasc. Ther. 12, 654-659.

13. Li, Z.; Kleinstreuer, C.; Farber, M. (2005) Biomech. Model. Mechanobiol. 4, 221-234.

14. Back, M.; Kopchok, G.; Mueller, M.; Cavaye, D.; Donayre, C.; White, R.A. (1994) J. Vasc. Surg. 19, 905-911.

15. Holzapfel, G.A.; Stadler, M.; Gasser, T.C. (2005) ASME J. Biomech. Eng. 127, 166-180.

16. Banerjee, R.K.; Back, L.H.; Cho, Y.I. (2001) in Computational fluid dynamics modeling techniques, using finite element methods to predict arterial blood flow, Biomechanical Systems Techniques & Applications: Biofluid Methods in Vascular and Pulmonary Systems, eds. Leondes, C. (CRC Press NY), Vol. 4, Chap. 8.

17. Attinger, F.M. (1968) Circ. Res. 22, 829-840.

18. Ogden, R.W. (2003) in Nonlinear elasticity, anisotropy, material stability and residual stresses in soft tissue, Biomechanics of soft tissue in cardiovascular systems, eds. Holzapfel, G. A. & Ogden, R.W. (Springer, NY), pp. 86-95.

19. Ehrlich, W.; Baer, R.W.; Bellamy, R.F.; Randazzo, R. (1980) Circ. Res. 47, 88-98.

20. Levy, M.N.; Brind, S.H.; Brandlin, F.R.; Phillips, Jr. F.A. (1954) Circ. Res. 2, 372-380.

21. Levy, M.N.; Share, L. (1953) Circ. Res. 1, 247-255.

22. Urzua, J.; Nunez, G., Lema, G.; Canessa, R.; Sacco, C. (1999) J. Clin. Monit. Comput. 15, 429-433.

23. Cox, R.H. (1975) Am. J. Physiol. 229, 1371-1375.

24. Van Loon, P. (1977) Biorheology. 14, 181-201.

25. ADINA Theory and Modeling Guide, Watertown, MA, 2004, Vols. I & III.

26. Caro, C.G.; Fitzgerald, J.M.; Schroter, R.C. (1971) Proc. Roy. Soc. London. 177, 109–159.

27. Cox, R.H. (1976) Am. J. Physiol. 230, 462–470.

28. Womersley, J.R. (1955) J. Physiol. 127, 553-563.

29. Pedley, T.J. (1980) in The fluid mechanics of large blood vessels, 1st edition, (Cambridge University Press NY).

30. Megerman, J.; Hasson, J.E.; Warnock, D.F.; L'Italien, G.J.; Abbott, W.M. (1986) Am. J. Physiol. Heart. Circ. Physiol. 250, H181-H188.

31. Fung, Y.C.; Fronek, K.; Patitucci, P. (1979) Am. J. Physiol. 237, H620-631.

32. Fung, Y.C. (1993) in Biomechanics, Mechanical properties of living tissues, 2nd edition, (Springer-Verlag, New York).